Phase Change Heat Transfer Simulation for Boiling Bubbles Arising from a Vapor Film by the VOSET Method

D. Z. Guo , D. L. Sun , Z. Y. Li & W. Q. Tao

Taylor & Francis
Taylor & Francis Group

PHASE CHANGE HEAT TRANSFER SIMULATION FOR BOILING BUBBLES ARISING FROM A VAPOR FILM BY THE VOSET METHOD

D. Z. Guo[1], D. L. Sun[2], Z. Y. Li[1], and W. Q. Tao[1]

[1]*Key Laboratory of Thermal Fluid Science and Engineering of MOE, School of Energy & Power Engineering, Xi'an Jiao Tong University, Xi'an, Shaanxi, People's Republic of China*
[2]*School of Renewable Energy, North China Electric Power University, Beijing, People's Republic of China*

This article presents a numerical method directed towards the simulation of flows with changes of phase. The volume-of-fluid level set (VOSET) method, which is a new interface capturing method and combines the advantages of both volume-of-fluid (VOF) and level set methods, is used for interface tracking. A difficulty occurs for the problems studied here: the discontinuous velocity field due to the difference between mass-weighted velocity and volume weighted velocity caused by the phase change at the interface. In this article, some special treatment is made to overcome this difficulty. The VOSET method and the developed treatment for the difference between mass-weighted and volume-weighted velocities are adopted to simulate a one-dimensional Stefan problem, two-dimensional horizontal film boiling, and horizontal film boiling of water at near critical pressure. The predicted results in both Nusselt number and flow patterns are agreeable with experimental results available in the literature.

1. INTRODUCTION

Boiling is a ubiquitous and important process in the extraction of energy from all kinds of sources, such as fossil, solar, and nuclear fuels due to the large amounts of energy in the form of latent heat. Despite decades of research, many details of the boiling physical process are still not well revealed [1, 2]. Researchers have found it to be extremely difficult to conduct accurate and effective boiling experimental measurements because of the small spatial scales and rapid time constants which are involved in the phase change process. With the rapid development of computer hardware and numerical algorithm in the last two decades, numerical simulations have become an important and useful method to investigate this kind of complex phenomenon.

NOMENCLATURE

a	thermal diffusivity	β	$= C_{pg}(T_{wall} - T_{sat})/h_{lg}$
C	volume fraction	χ	dimensionless wall heat flux
c_p	specific heat at constant pressure	δt	time step
d	distance function	Δx	length step
f	wetted portion	φ	level set function
$\vec{g}$	acceleration gravity	γ(t)	interface
h_{lg}	latent heat of vaporization	κ	curvature
$\vec{n}$	outward unit normal vector	$λ_0$	wavelength
p	pressure	μ	dynamic viscosity
q	heat flux	ρ	density;
$\vec{r}$	radius vector	σ	surface tension coefficient
S	surface area	Ω	volume source (sink)
$\vec{S}$	surface area vector		
t	time	**Subscripts**	
T	temperature	g	gas
$\vec{u}$	velocity vector	l	liquid
V	volume	sat	saturation
x,y	coordinates	wall	wall

At the numerical simulation aspect, boiling heat transfer is one among the difficult challenges for numerical simulations owing to its many influencing factors, including solid surface structure, surface tension, the discontinuous flow properties across the phase interface, and complicated phase interface dynamics. For gas–liquid interface physics, recent studies have provided various numerical schemes including interface capturing and interface tracking to handle these problems. To the best knowledge of the authors, the first attempt at numerical boiling simulation can be attributed to Son and Dhir [1], who used the Lagrangian method to track the interface. However, they just focused on the evolution of the bubble after the detachment and did not obtain the result of the whole interfacial motion. Later Juric and Tryggvason [2] extended the front tracking method [3] to simulate horizontal film boiling using source terms in the continuity equation. Son and Dhir [4] applied the level set approach [5] to the model of boiling flow and offered more details about bubble release pattern during horizontal film boiling. Their research shows the great potential of the interface-capturing methods in the numerical study of the boiling heat transfer process.

As far as the interface-capture methods are concerned, the original level set approach has one severe disadvantage in that conservation of liquid mass cannot be guaranteed [6–8]. The volume-of-fluid (VOF) method [9] and its variants [10, 11] can satisfy the mass conservation requirement. One drawback of the VOF method, however, is the difficulty to obtain an accurate curvature and to smooth the discontinuous physical quantities near the interfaces. Therefore, in some sense these two interface-capture methods are compensatory to each other. In recent years, some approaches appear to couple the level set and VOF method in order to overcome the disadvantages of the two methods. The CLSVOF method introduced by Bourlioux [13] and further developed by Sussman and Puckett [6] is such an example. Tomar et al. [12] adopted this method to investigate the bubble growth in water at

near critical pressure for different degrees of superheat. Although this method extracts the advantages of VOF and level set methods, it is computationally more complicated than both of them. In this method, both the C (the major variable in VOF) and ϕ (the major variable in level set) advection equations need to be solved. Another approach proposed by Sun and Tao is called VOSET [14]. Its implementation process is simpler than the CLSVOF. In this method, only the C advection equation needs to be solved by the VOF method which has strong abilities to simulate the deformations of the interface including break-up and coalescence, and the level set function ϕ is calculated by a simple iterative geometric operation and is used to calculate some geometric parameters and fluid properties at the interface, thus leading to a significant simplification of solution process.

In the present work, the volume-of-fluid level set (VOSET) method [14] is used to capture interfaces for computing two-phase flows in film boiling. In particular, we use some special treatments to deal with the discontinuous velocity field due to phase change at the interface. The one-dimensional Stefan problem is adopted as a test to demonstrate the rationality and validity of these measures. Then, we apply this method to the simulation of two-dimensional thin boiling films. The horizontal film boiling of water at near critical pressure has also been simulated.

2. MATHEMATICAL FORMULATIONS

2.1. Volume Fraction Function

The VOF method is a fixed-grid technique for two or more fluids which are not interpenetrating. The location of the phase interface is determined by tracking of the volume fraction C of each fluid in computational cells. The volume fraction C was proposed by Hirt and Nichols [9] in 1981, and the C advection equation needs to be solved in order to identify each phase separately. This method has strong abilities to track the free surface of the fluid everywhere in flows. In this study, in order to distinguish two phases, the volume fraction of the gas phase shall be

$$C = \begin{cases} 1 & \text{if the cell is completely filled by gas phase} \\ 0 < C < 1 & \text{if the cell contains part of the interface} \\ 0 & \text{if the cell is completely filled by liquid phase} \end{cases} \tag{1}$$

In each cell, the sum of the volume fraction of all phases should be unity. For a given flow field, the standard advection equation governs the evolution of C.

$$\frac{\partial C}{\partial t} + \vec{u} \cdot \nabla C = 0 \tag{2}$$

Assuming that the flow field is incompressible, then the C advection equation can be recast in the conservative form.

$$\frac{\partial C}{\partial t} + \nabla \cdot (\vec{u}C) = 0 \tag{3}$$

For the numerical solution of the C advection equation, the standard finite-difference approximations would lead to a smearing of the C function and the interfaces would lose their definition. Therefore, the volume tracking algorithms are applied to capture the interfaces. Most volume tracking algorithms published to date fall into one of these two interface reconstruction categories: one is the piecewise constant volume tracking method, which includes Hirt and Nichols's donor-acceptor algorithm [9]; and the other is the piecewise linear volume tracking method, which includes the piecewise linear interface construction (PLIC) algorithm due to Youngs [11]. In our study, the PLIC algorithm is adopted to reconstruct the interfaces because this algorithm is more accurate than the other algorithms. The reconstruction is done based on geometrical calculations and determines the liquid and gas fluxes across cell faces. As indicated above, the advantage of the VOF method is that the mass can be conserved while still maintaining sharp interfaces [6]. However, because the volume fraction function C is a step function, it is difficult to obtain the accurate curvature and smooth the discontinuous physical quantities near the interfaces. It is in this regard that the level set (LS) method can play an important role.

2.2. Level Set Function

In the LS method [15], a smooth function ϕ called the level set function is used to represent the interface. Generally, the signed distance function, on which an extra condition of $|\nabla\phi| = 1$ is imposed, is defined as the level set function. The signed distance function for a point can be expressed as

$$\phi(\vec{r}, t) = \begin{cases} -d(\vec{r}, \Gamma(t)) < 0, & \text{if } \vec{r} \in \text{the gas phase} \\ = 0, & \text{if } \vec{r} \in \text{the interface} \\ d(\vec{r}, \Gamma(t)) > 0 & \text{if } \vec{r} \in \text{the liquid phase} \end{cases} \tag{4}$$

where $\Gamma(t)$ denotes the interface, and d is the distance function which is the shortest distance from the point in consideration to the interfaces. According to the above definition, the point location is indicated by $\phi < 0$ if it is in the dispersed-phase region, $\phi > 0$ in the continuous-phase region, and $\phi = 0$ on the interfaces.

The unit normal vector $\vec{n}$ of the interface is

$$\vec{n} = \frac{\nabla\phi}{|\nabla\phi|} \tag{5}$$

The curvature κ can be obtained by the following equation.

$$\kappa = \left(\nabla \cdot \frac{\nabla\phi}{|\nabla\phi|}\right) \tag{6}$$

The curvature defined by the above equation can be computed accurately due to the fact that ϕ is a continuous function.

2.3. Governing Equations

For viscous incompressible two-phase flows with constant thermophysical properties, the Navier-Stokes equations can describe both phases by the set of the following expressions.

$$\nabla \cdot \vec{u} = 0 \tag{7}$$

$$\rho\left(\frac{\partial \vec{u}}{\partial t} + \vec{u} \cdot \nabla \vec{u}\right) = -\nabla p + \nabla \cdot [\mu((\nabla\vec{u}) + (\nabla\vec{u})^{\mathrm{T}})] + \rho\vec{g} \tag{8}$$

$$\frac{\partial T}{\partial t} + \vec{u} \cdot \nabla T = \frac{\lambda}{\rho c_p}\nabla^2 T \tag{9}$$

Here, $\vec{g}$ is the acceleration of gravity and $\vec{u}$, p, c_p, T, ρ, λ, and μ are the fluid velocity vector, pressure, specific heat, temperature, density, conductivity, and viscosity, respectively.

Around the interface, the momentum equation should be modified when the surface tension force should be taken into account. Based on the continuum surface force (CSF) model [16] and the level set function, the momentum equation can be expressed as follows.

$$\rho(\phi)\left(\frac{\partial \vec{u}}{\partial t} + \vec{u} \cdot \nabla \vec{u}\right) = -\nabla p + \nabla \cdot [\mu(\phi)((\nabla\vec{u}) + (\nabla\vec{u})^{\mathrm{T}})] + \rho(\phi)\vec{g} + \sigma\kappa(\phi)\nabla H(\phi) \tag{10}$$

Here, $\vec{u}$ is the mass average velocity and σ is the surface tension factor. For smoothing the discontinuous physical quantities near interfaces, the smoothed Heaviside function is used which is given by

$$H(\phi) = \begin{cases} 0 & \text{if } \phi < -\varepsilon \\ \frac{1}{2}\left[1 + \frac{\phi}{\varepsilon} - \frac{1}{\pi}\sin(\pi\phi/\varepsilon)\right] & \text{if } |\phi| \leq \varepsilon \\ 1 & \text{if } \phi > \varepsilon \end{cases} \tag{11}$$

where ε denotes the width of transition region used for smoothening.

Then, the smoothed density and viscosity can be calculated by

$$\rho(\phi) = \rho_g(1 - H(\phi)) + \rho_l H(\phi) \tag{12}$$

$$\mu(\phi) = \mu_g(1 - H(\phi)) + \mu_l H(\phi) \tag{13}$$

The subscripts g and l represent gas and liquid, respectively.

The determination of the level set function within the transition region is conducted via some simple iterative geometrical operations instead of solving the level set advection equation, as indicated above. More details about the VOSET method can be found in reference [14].

2.4. Mass Transfer

At the interface there is a jump of density and velocity due to the phase change. For a computational cell with an interface, the mass balance equation for each phase can be expressed as follows.

$$\frac{d}{dt}\int_{V_g(t)}\rho_g dV + \int_{S_g(t)}\rho_g\vec{u}\cdot\vec{n}dS + \int_{S_I(t)}\rho_g(\vec{u}-\overrightarrow{u_I})\cdot\vec{n}dS = 0 \tag{14}$$

$$\frac{d}{dt}\int_{V_l(t)}\rho_l dV + \int_{S_l(t)}\rho_l\vec{u}\cdot\vec{n}dS + \int_{S_I(t)}\rho_l(\vec{u}-\overrightarrow{u_I})\cdot\vec{n}dS = 0 \tag{15}$$

Here, $V_g(t)$, $S_g(t)$, $V_l(t)$, and $S_l(t)$ are the volumes and surface area of the cell boundary at the liquid region and the vapor region, respectively. $\vec{n}$ is the normal vector of the phase interface $S_I(t)$ and points into the liquid phase. $\overrightarrow{u_I}$ is the interface velocity vector. As both phases are assumed to be incompressible and the whole volume of the computational cell is constant, combining Eqs. (14) and (15), we can obtain

$$\int_{S_C}\vec{u}\cdot\vec{n}dS + \int_{S_I(t)}\|(\vec{u}-\overrightarrow{u_I})\|\cdot\vec{n}dS = 0 \tag{16}$$

where $|\cdot|$ represents the jump of the item within the symbol across the interface [12], and S_C represents the boundary of the cell. At the interface, the mass transfer condition can be expressed as

$$\|\rho(\vec{u}-\overrightarrow{u_I})\|\cdot\vec{n} = 0 \tag{17}$$

The energy jump condition can be expressed as

$$\|\rho h(\vec{u}-\overrightarrow{u_I})\|\cdot\vec{n} + \|\vec{q}\|\cdot\vec{n} = 0 \tag{18}$$

From Eqs. (17) and (18), the velocity jump term is determined by

$$\|(\vec{u}-\overrightarrow{u_I})\|\cdot\vec{n} = \frac{\|\vec{q}\|\cdot\vec{n}}{h_{lg}}\left(\frac{1}{\rho_g}-\frac{1}{\rho_l}\right) \tag{19}$$

Here, $\vec{q}$ is the heat flux vector at the interface and h_{lg} is the latent heat of vaporization.

By substituting Eqs. (10) to (20), we can obtain

$$\int_{S_C}\vec{u}\cdot\vec{n}dS + \int_{S_I(t)}\frac{\|\vec{q}\|\cdot\vec{n}}{h_{lg}}\left(\frac{1}{\rho_l}-\frac{1}{\rho_g}\right)dS = 0 \tag{20}$$

That is

$$\int_{V_C}\Omega dV = \int_{S_I(t)}\frac{\|\vec{q}\|\cdot\vec{n}}{h_{lg}}\left(\frac{1}{\rho_g}-\frac{1}{\rho_l}\right)dS \tag{21}$$

where $\Omega = \nabla \cdot \vec{u}$ is the volume source or sink caused by phase change. V_C is the volume of a cell. From this equation, it can be seen that at the interface of the two-phase flow the divergence-free condition of the velocity field is no longer satisfied due to new volume generated by evaporation or volume vanished by condensation, even though both gas and liquid are incompressible fluids.

In the VOSET method the advection equation of C is solved to track the interface. The direct application of PLIC to solve this advection equation requires that the velocity is volume conservative. However, in the above derivation $\vec{u}$ is the mass-averaged velocity vector and therefore is generally not volume conservative. So, we should use some methods to avoid this problem. According to [17], the definitions of the volume-weighted and mass-weighted velocity are described as follows.

$$v_{\text{vol}} = v_l f + v_g (1 - f) \tag{22}$$

$$v_\rho = \frac{v_l f \rho_l + v_g (1 - f) \rho_g}{f \rho_l + (1 - f) \rho_g} \tag{23}$$

where v_{vol} being the volume-weighted velocity, v_ρ the mass-weighted velocity, and f the wetted portion of each face of the cell.

From the definitions of two kinds of velocities, we can see that they are very different in most cases. In order to calculate the fluxes across the interface more accurately, we should transfer the mass-weighted velocity to the volume-weighted one by which the VOF method can be applied. The treatment of this part will be described in detail in the following section.

3. NUMERICAL METHODS

3.1. Discretization of Governing Equations

The spatial discretization of the momentum equations is based on the finite volume method (FVM) [18, 19] by using a staggered arrangement of the variables. Velocity is located at cell edges and all other scalars are located at cell centers. The MUSCL upwind differencing [20] is adopted for the convection term and the central differencing for the viscous and curvature terms.

The transient energy equation is first solved in the bulk phases explicitly.

$$T^{n+1} = T^n + \delta t \left(\frac{\lambda}{\rho c_p} \nabla^2 T - \vec{u} \cdot \nabla T \right)^n \tag{24}$$

In the liquid region and at the interface, the temperature is assumed to be equal to saturation temperature T_{sat}. Only the temperature field of gas phase needs to be solved. The interface of gas and liquid can be viewed as the boundary of the gas region. In order to solve the temperature field, the temperature at the center of the cell which includes an interface is obtained by linear interpolation.

After the new temperature field is obtained, the interfacial heat flux included in the mass source term can be calculated. The continuity and momentum equations

discretized at the time direction are

$$\int_{s_c} \vec{u}^{n+1} \cdot \vec{n} ds + \int_{s_l(t)} \left(\frac{1}{\rho_l} - \frac{1}{\rho_g} \right) \frac{\|\vec{q}^{n+1}\| \cdot \vec{n}}{h_{lg}} ds = 0 \qquad (25)$$

$$\frac{\vec{u}^{n+1} - \vec{u}^n}{\delta t} + \vec{u}^{n+1} \nabla \cdot (\vec{u}^{n+1}) = \frac{1}{\rho(\phi^{n+1})} \{ -\nabla p^{n+1} + \nabla \cdot \eta(\phi^{n+1})$$
$$[(\nabla \vec{u}^{n+1}) + (\nabla \vec{u}^{n+1})^T] + \rho(\phi^{n+1}) \vec{g} + \sigma \kappa(\phi^{n+1}) \nabla H(\phi^{n+1}) \} \qquad (26)$$

A robust and efficient algorithm called IDEAL, by Sun et al. [21, 22], is adopted to treat the pressure-velocity coupling. The pressure equations are solved by using a Krylov subspace method: the Bi-CGSTAB method proposed by Van Der Vorst [23, 24]. When the velocity field is obtained, Young's method is employed to calculate the C function and the new location of interface and level set function ϕ can be obtained.

In this article, we cope with the energy equation by the explicit scheme. Hence, the scheme has a time step restriction. For the advective transport, the CFL stability condition is followed. The diffusive transport stability constraint is

$$\frac{2\lambda \Delta t}{\rho c_p \Delta x^2} \le 1 \qquad (27)$$

The capillary time step constraint is [17]

$$\frac{2\sqrt{\sigma \pi \Delta t / (\rho_l + \rho_g)}}{\Delta x^{3/2}} \le 1 \qquad (28)$$

3.2. Interface Velocity and Jump Conditions

As indicated above, the mass-weighted and volume-weighted velocities are different. Here, their relationship is discussed in detail. The velocity field across the interface is not continuous due to the volume change inherent to the phase change. Thus, the velocity at the interface is directly related to the volume change. A simple case is considered in Figure 1a. This case describes a cell including an interface which is parallel to the x-axis. Its right face is fully gaseous and its left face is completely wetted. On the right face, the fluid velocity is $u_{g,i+1}$ and on the left face the fluid velocity is $u_{l,i}$. For these two velocities, the mass-averaged and volume-averaged velocities are equal. Velocities on other faces are defined zeros. Thus, we can simply obtain the following relationship.

$$u_{g,i+1} - u_{l,i} = \Omega \Delta x_i \qquad (29)$$

where Δx_i is the edge length of cell i in the direction of the x-axis. In this situation we can easily understand the effect of volume source on the velocity components, which are perpendicular to the interface. A more general and complex situation is described in Figure 1b. It is obvious that for this case the mass-averaged and volume-averaged velocities are not identical since the faces are partially wetted. The derivation process for the relationship between them is presented below.
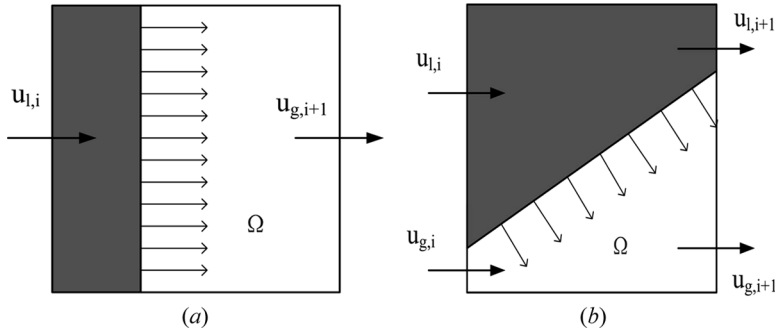
Figure 1. Velocities of the gas and liquid. (*a*) Case I and (*b*) case (II).

As the discontinuity of velocity is caused by the volume source, it is obvious to obtain the following expression in the x direction of Figure 1*b*.

$$\frac{u_{g,i+1} - u_{l,i+1}}{\Delta x_i}(1 - f_{i+1/2}) = \Omega n_x \tag{30}$$

where Ωn_x is the projection of Ω in the x direction.

Then combining Eqs. (23) with (30), we can obtain equations for $u_{l,i+1}$ and $u_{g,i+1}$.

$$u_{l,i+1} = u_\rho - \frac{\Omega n_x \Delta x_i \rho_g}{f_{i+1/2}\rho_l + (1 - f_{i+1/2})\rho_g} \tag{31}$$

$$u_{g,i+1} = u_\rho + \frac{\Omega n_x \Delta x_i \rho_l}{f_{i+1/2}\rho_l + (1 - f_{i+1/2})\rho_g}\frac{f_{i+1/2}}{1 - f_{i+1/2}} \tag{32}$$

In Eqs. (31) and (32), u_ρ is the mass-weighted velocity obtained by the pressure equation. We can also make similar derivation in the y-direction. Within the cell, the liquid velocity is assumed not changed and only the gas velocity has a change after evaporation. And they should be equal on one face if no evaporation happened. Simultaneously, the mass-weighted and volume-weighted velocities are both equal to $u_{l,i+1}$, and the divergence-free condition of the velocity field of the cell with an interface is satisfied too. Hence, we can directly apply the VOF method to calculate the location of the interface only if the part of the liquid which is evaporated to gas is subtracted. This treatment, however, would bring the volume imbalance of neighboring cells. Therefore, corresponding components of the evaporation volume should be compensated to the neighboring cells.

4. NUMERICAL RESULTS

4.1. One-Dimensional Test Case

The one-dimensional Stefan problem is a classic case to test the two-phase flow with phase change. In the problem, the vapor experiences an increase of temperature

at the wall which drives mass transfer at the interface. The vapor will keep motion-less while the liquid and the interface would be driven away from the wall in this flow, as shown in Figure 2. The formulation for the gas phase of one-dimensional Stefan problem can be expressed as

$$\frac{\partial T}{\partial t} = a\frac{\partial^2 T}{\partial x^2} \quad 0 \le x \le \delta(t) \tag{33}$$

where $\delta(t)$ is the interface location. The boundary conditions are

$$\begin{array}{ll} T = T_{\text{wall}} & \text{at } x = 0 \\ T = T_{\text{sat}} & \text{for } x \ge \delta(t) \\ \rho_g \frac{\partial \delta}{\partial t} h_{\text{lg}} = -k\frac{\partial T}{\partial x} & \text{at } x = \delta(t) \end{array} \tag{34}$$

The exact interface location $\delta(t)$ of the one-dimensional Stefan problem [25] has been given by

$$\delta(t) = 2\zeta\sqrt{at} \tag{35}$$

where ζ is the solution to the transcendental equation

$$\zeta\exp(\zeta^2)erf(\zeta) = \frac{c_{pg}(T_{\text{wall}} - T_{\text{sat}})}{h_{lg}\sqrt{\pi}} \tag{36}$$

The normal liquid velocity caused by phase change is obtained by

$$v_l(t) = \frac{\partial \delta}{\partial t}\left(1 - \frac{\rho_g}{\rho_l}\right) \tag{37}$$

In this simulation, we consider three different kinds of density ratios $\rho_l/\rho_g = 10$, 100, and 1000, with the relative values of α being 2.5×10^{-4}, 2.5×10^{-3}, and
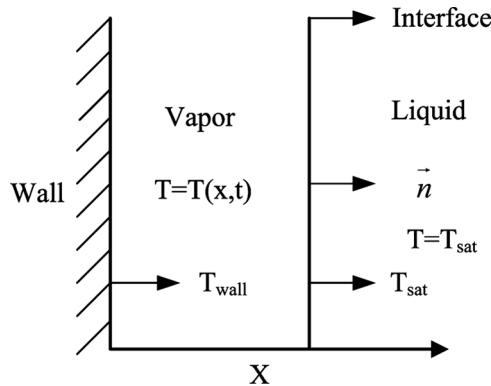

Figure 2. Sketch map of Stefan problem.

2.5×10^{-2}, respectively. Latent heat $h_{lg} = 10000\,\mathrm{J/kg}$ and $c_{pg} = 200\,\mathrm{J/(kg \cdot K)}$. The temperature of solid boundary is set $10\,\mathrm{K}$ higher than the saturation temperature. The simulation is conducted on a grid with 50 nodes. In the beginning, one cell is set to be full of vapor and the initial interface is included in the second cell.

Figure 3 shows the interface position and the liquid velocity which evolves with time. The simulation results agree with the exact solution excellently despite the relatively small number of nodes and so few vapor cells to be set in the early stage.

4.2. Two-Dimensional Horizontal Film Boiling

Now, we turn to the two-dimensional film boiling problem. In this process, there exists a layer of vapor which is located below a layer of liquid and fully covers a heated solid boundary. The Rayleigh-Taylor instability of the liquid-vapor interface is resulted from gravity. With the evaporation of the liquid and the generation of fresh vapor near the solid boundary, the liquid is prevented from contacting the

(a)

(b)
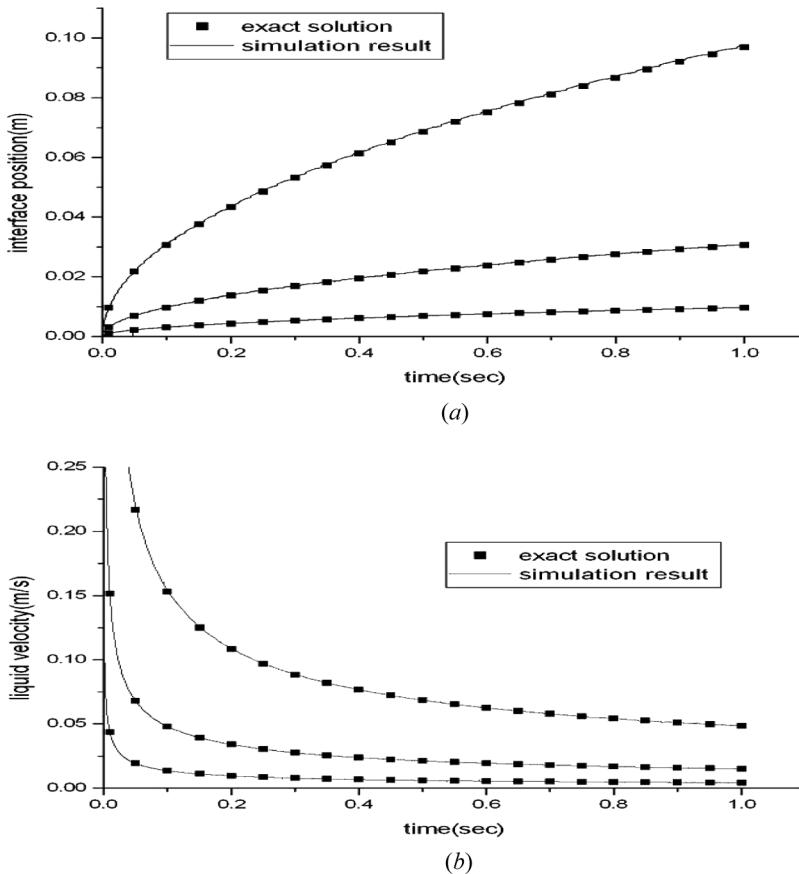
Figure 3. Numerical simulation results for 1-D Stefan problem. From top to bottom, density ratios are 1000, 100, and 10, respectively. (a) Interface position and (b) liquid velocity.

wall and more vapors are provided to the rising bubbles. Then, the liquid falls toward the wall while the vapor rises away from it. A balance is achieved between vapor generation by evaporation at the interface and vapor removal by the break off and rise of bubbles.

There are a lot of correlations to describe the complex mechanism of a horizontal film boiling. Among these models, the most widely accepted one is suggested by Berenson [26]. He assumes that vapor bubbles are placed in a square pattern with a spacing equal to the most dangerous Taylor wavelength given by

$$\lambda_0 = 2\pi\sqrt{\frac{3\sigma}{(\rho_l - \rho_g)g}} \tag{38}$$

Combining the further assumption that the mean bubble height and diameter are proportional to the bubble spacing and ignoring the convective energy transport, he also obtained an expression for the Nusselt number as

$$\text{Nu} = 0.425\left(\frac{\rho_g(\rho_l - \rho_g)gh_{lg}}{\lambda_g\mu_g(T_{\text{wall}} - T_{\text{sat}})}\right)^{1/4}(\lambda')^{3/4} \tag{39}$$

where λ' is the characteristic length and given by

$$\lambda' = \sqrt{\frac{\sigma}{(\rho_l - \rho_g)g}} \tag{40}$$

In 1981, Klimenko [27] carried out a somewhat generalized analysis of film boiling on horizontal plates based on some basic assumptions similar to Berenson's. His correlation for Nu is expressed as follows

$$\text{Nu} = \begin{cases} 0.19 \times \text{Gr}^{1/3}\text{Pr}^{1/3}f_1 & \text{for Gr} < 4.03 \times 10^5 \\ 0.0216 \times \text{Gr}^{1/2}\text{Pr}^{1/3}f_2 & \text{for Gr} > 4.03 \times 10^5 \end{cases} \tag{41}$$

where

$$f_1 = \begin{cases} 1 & \text{for } \beta > 0.71 \\ 0.89\beta^{-1/3} & \text{for } \beta < 0.71 \end{cases} \tag{42}$$

$$f_2 = \begin{cases} 1 & \text{for } \beta > 0.50 \\ 0.71\beta^{-1/2} & \text{for } \beta < 0.50 \end{cases} \tag{43}$$

In the equations the Grashof number, Prandlt number, and β are expressed as

$$\text{Gr} = \frac{\rho_g^2 g\lambda'}{\mu_g^2}\left(\frac{\rho_l}{\rho_g} - 1\right) \tag{44}$$

$$\text{Pr} = \frac{C_{pg}\mu_g}{\lambda_g} \tag{45}$$

$$\beta = \frac{C_{pg}(T_{\text{wall}} - T_{\text{sat}})}{h_{lg}} \tag{46}$$

Klimenko's correlation suggests that for small values of β, the heat transfer coefficient varies with $(T_{\text{wall}} - T_{\text{sat}})^{-1/3}$ or $(T_{\text{wall}} - T_{\text{sat}})^{-1/2}$ depending on Gr. For high values of β, the heat transfer coefficient is independent of wall superheat. The deviations between experimental data and this analytical solutions for Nusselt number are within ± 25 percent, which is better than Berenson's model. Thus, in this study we will compare our simulation results with Klimenko's correlation.

Now, an example of a two-phase fluid flow is considered with the following parameters. The vapor parameters are $\lambda_g = 1.0\,\text{W/(m} \cdot \text{K)}$, $\mu_g = 0.005\,\text{Pa} \cdot \text{s}$, $c_{pg} = 200.0\,\text{J/(kg} \cdot \text{K)}$, and $\rho_g = 5.0\,\text{kg/m}^3$, whereas the liquid properties are $\lambda_l = 40.0\,\text{W/(m} \cdot \text{K)}$, $\mu_l = 0.1\,\text{Pa} \cdot \text{s}$, $c_{pl} = 400.0\,\text{J/(kg} \cdot \text{K)}$, and $\rho_l = 200.0\,\text{kg/m}^3$. Surface tension is $\sigma = 0.1$ N/m, latent heat is $h_{lg} = 10000.0\,\text{J/kg}$, and saturation temperature is $T_{\text{sat}} = 0\,\text{K}$. We select a rectangular region as the computational domain which is periodic in the x-direction. Its width is the most unstable Taylor wavelength λ_0 and its height is λ_0 or $3\lambda_0$. The top boundary is open and the fluid is allowed to exit. The bottom boundary is set to be a no-slip wall and both the left and right vertical boundaries are symmetrical. Figure 4 describes the details of the computational domain and boundary conditions. The liquid is initialized to be at the saturation state and the vapor temperature increases linearly from the liquid–vapor interface to the wall. The temperature of the solid wall is kept at 5 K above the saturation temperature. The interface location is initialized as

$$y = \frac{\lambda_0}{128}\left(4.0 + \cos\left(\frac{2\pi x}{\lambda_0}\right)\right) \tag{47}$$
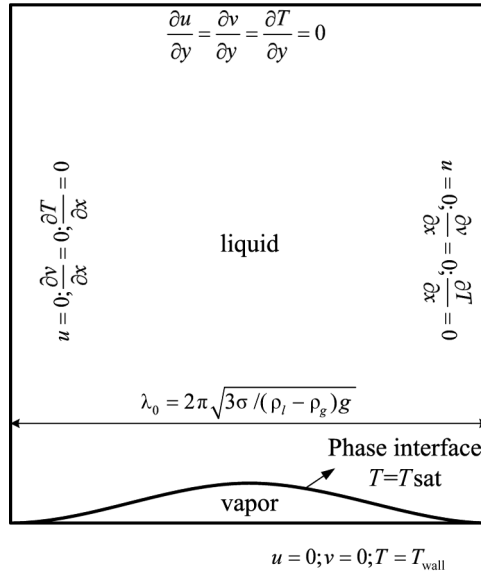

Figure 4. Computational domain and boundary conditions.

In order to obtain grid-independent results, we consider three different grid systems of 32×32, 64×64, and 128×128. Figure 5 depicts the interface computed on the three grids as the first bubble is going to detach from the film and the vapor volume relative to the initial vapor volume. According to these figures, we find that the 64×64 grid system can adequately represent this case. Thus, we use this grid to make the later simulation.

Film boiling is a quasi-steady phenomenon, whose behavior was studied previously by Welch and Wilson [10] and Gibou et al. [28]. Figure 6a shows the early transients typified by the release of a few larger bubbles before arriving at the quasi-steady bubble release pattern, which is illustrated in Figure 6b. The results are consistent with those presented in references [10, 28]. The local Nusselt number is obtained by

(a)

(b)
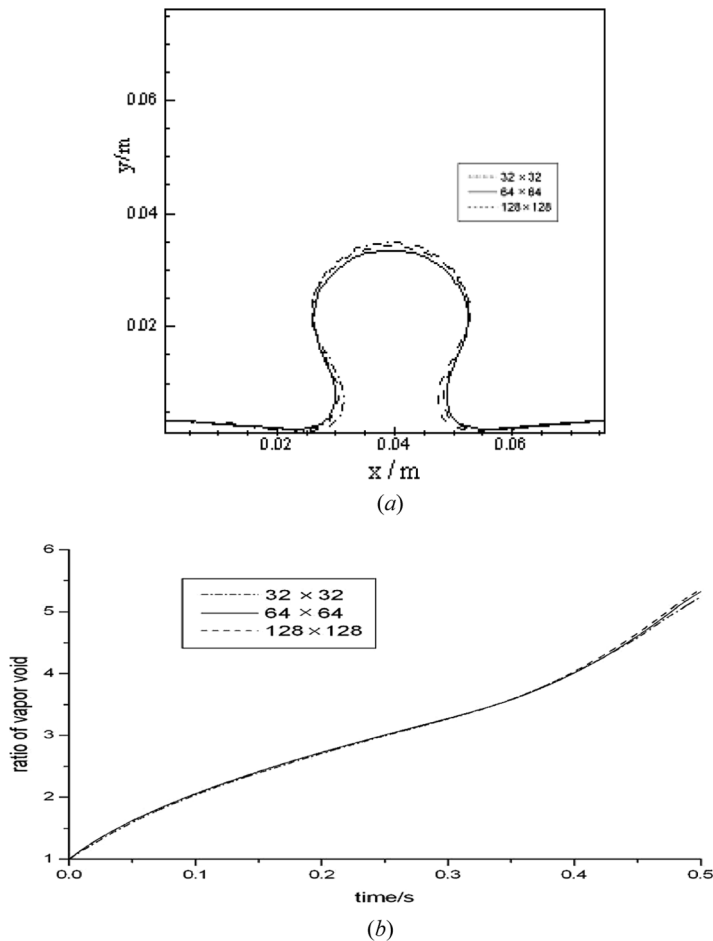
Figure 5. Simulation results for three grid systems. (a) Bubble shape at $t = 0.43$ s and (b) ratio of vapor void to initial vapor void.
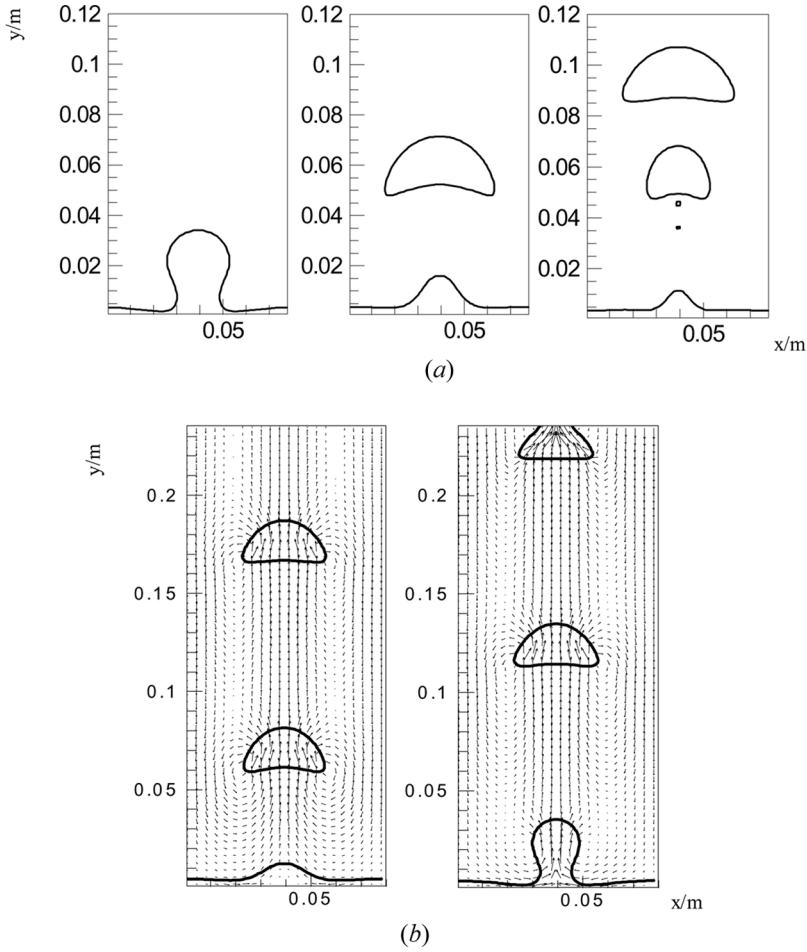
Figure 6. Simulation results at different time instants. (*a*) The release of bubbles at early instant of $t = 0.44$ s, 0.605 s, and 0.77 s, respectively; (*b*) the quasi-steady bubble release pattern and velocities at $t = 1.65$ s and 1.80 s, respectively.

$$\mathrm{Nu} = \frac{\lambda'}{(T_{\mathrm{wall}} - T_{\mathrm{sat}})} \frac{\partial T}{\partial y}\bigg|_{y=0} \tag{48}$$

Figure 7 shows a space-averaged Nusselt number. The space- and time-averaged value is 1.73. According to Klimenko's correlation, the Nusselt number is 1.91. The difference between them is 9.42%.

The above simulation exhibits the quasi-steady behavior in a steady pattern of bubble release in which vapor bubbles leave the thin film. Juric and Tryggvason [2] obtained different behavior phenomenon with respect to bubble release. According to their example, hot vapor is much more quickly convected up into a mushroom shaped bubble which does not pinch off of its stem. Here, we obtain similar results
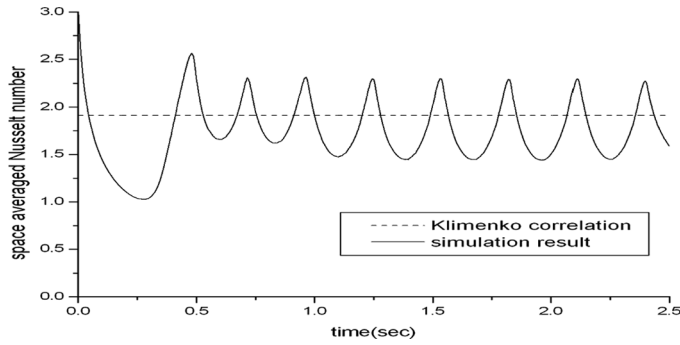
Figure 7. Simulation results for Nusselt number.

with the same fluid properties in reference [2]. By defining the following scales for length, velocity, temperature and heat flux

$$l_0 = \left(\frac{\mu_l^2}{g\rho_l^2} \right)^{1/3} \quad (l_0 g)^{1/2} \quad \frac{\rho_g h_{lg}}{\rho_l C_{pl}} \quad \frac{\rho_g h_{lg} \lambda_l}{\rho_l C_{pl} l_0}$$

the problem can be characterized by the Morton number Mo, the Prandtl number Pr, and a capillary parameter Ca.

$$\text{Mo} = \frac{\mu_l^4 g}{\sigma^3 \rho_l} \quad \text{Pr} = \frac{\mu_l C_{pl}}{\lambda_l} \quad \text{Ca} = \frac{C_{pl} \sigma T_{\text{sat}}}{\rho_g h_{lg}^2 l_0}$$

The computation parameters are

$$\frac{\rho_l}{\rho_g} = 5.22 \quad \frac{\mu_l}{\mu_g} = 3.37$$

$$\frac{\lambda_l}{\lambda_g} = 3.42 \quad \frac{C_{pl}}{C_{pg}} = 0.882$$

$$\text{Mo} = 1.0 \times 10^{-6} \quad \text{Pr} = 1.51 \quad \text{Ca} = 0.024$$

The results presentation of this example will be conducted by dimensionless quantities. We use a 64×320 grid system to simulate this case and the convergence criterion is the same with the previous simulation. The boundary conditions are also identical with the above case except for the bottom boundary, where dimensionless wall heat flux $\chi_w = 20.0$ is set up instead of constant wall temperature and the initial temperature field of the whole computational domain is set to be zero. The interface location is initialized as

$$Y = 24.0 - 3.8 \cos (2\pi X / \lambda_0) \tag{49}$$

Figure 8a depicts the interface plots as well as the temperature and velocity field at three different time instants. These results are consistent with the ones obtained in reference [2]. Figure 8b shows the Nusselt number compared with the analytical

(a)

(b)
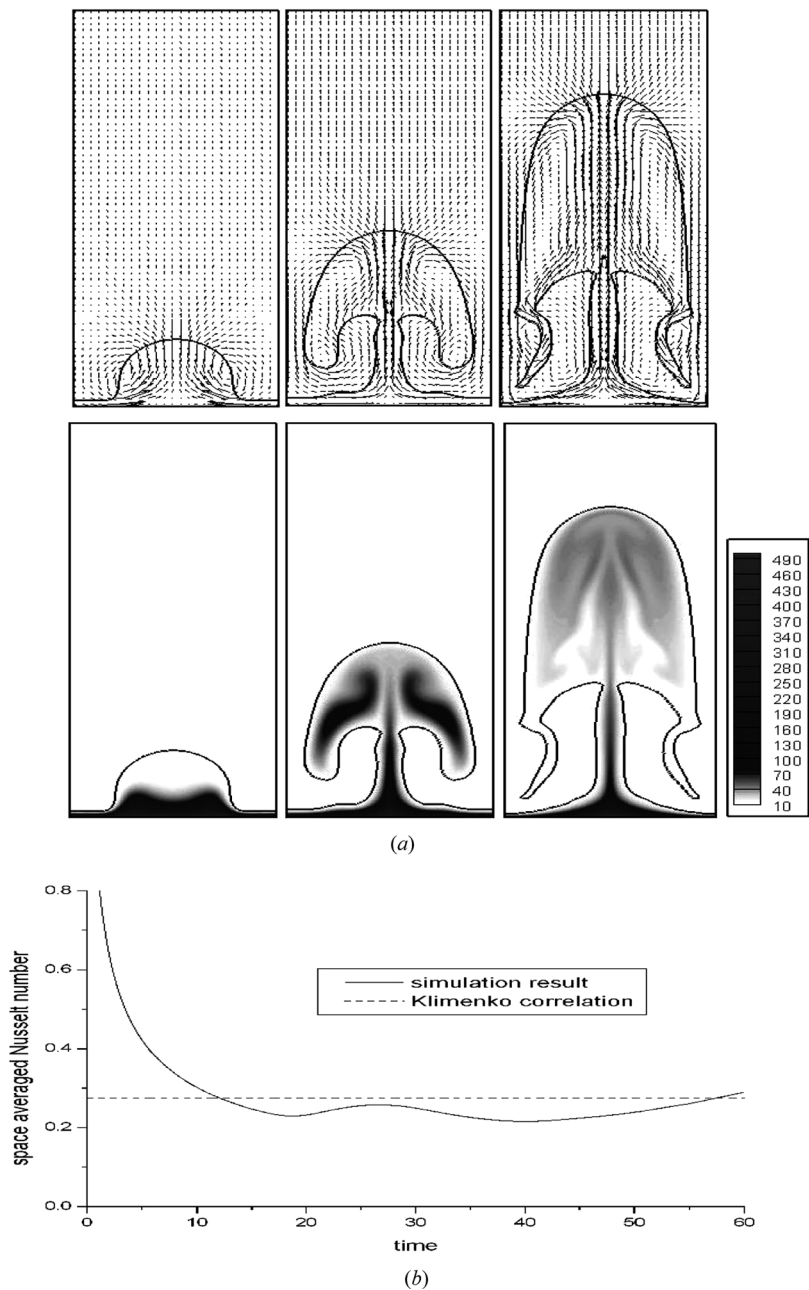
Figure 8. Simulation results for $\chi_w = 20$. (a) Simulation results at $tc = 20.11$, 39.82, and 58.33, respectively (top: velocity; bottom: temperature field); and (b) Nusselt number as the function of dimensionless time.

correlations. The value of analytical correlations is 0.275. The space- and time-averaged Nusselt number of numerical simulation is 0.264. The difference is 4.00%. If the results of the early stage are removed, the difference should be a bit larger.

Then, the wall heat flux χ_w is reduced to be 10 and other computational conditions are not changed. We make this simulation and obtain the results of the bubble's shapes as in Figure 9a. From this figure, it can be seen that the shapes of the bubble at $tc = 20.11$ and $tc = 39.82$ are almost the same with the bubble when the wall heat flux is $\chi_w = 20$ (Figure 8a). It should be noted that just the shapes are similar, while their sizes are different. When $tc = 58.33$, the bubbles of the two wall heat fluxes show quite different behaviors. For the lower wall heat flux, the bubble breaks and releases some small fragments when it grows to some extent. This bubble break may be caused by insufficiency of vapor supply generated at the wall surface. Obviously, the generation rate of vapor under the condition of the lower wall heat

(a)

(b)
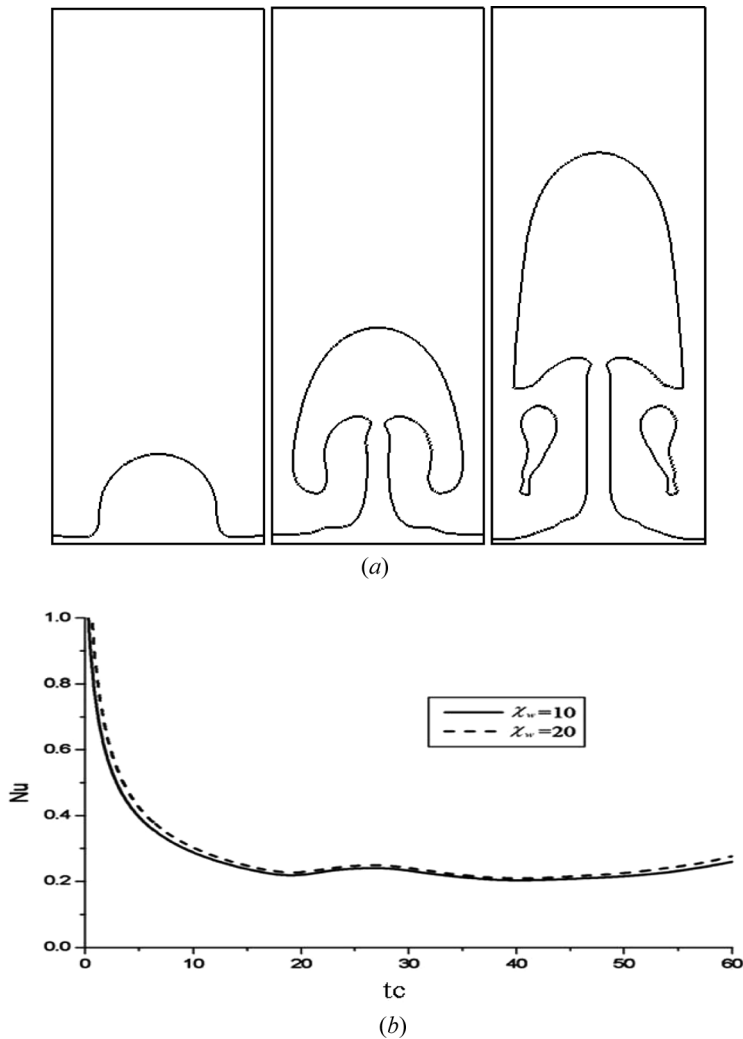
Figure 9. Simulation results for $\chi_w = 10$. (a) Bubble's shape at $tc = 20.11$, 39.82, and 58.33; and (b) the space-averaged Nusselt number for $\chi_w = 20$ and $\chi_w = 10$.

flux is smaller than the higher heat flux condition. Figure 9b describes the history of Nusselt number variation with time for $\chi_w = 20$ and $\chi_w = 10$. The result shows that the Nusselt numbers for the two cases are almost the same. The time- and space-averaged Nusselt number are 0.251 and 0.264 for $\chi_w = 10$ and $\chi_w = 20$, respectively. The difference is only about 5%. This means that the Nusselt number is not sensible to the heat flux in our cases. This result also agrees with Klimenko's correlation. In our simulations, the values of β ($\beta = \frac{c_{pg}(T_{wall} - T_{sat})}{h_{lg}}$) for both cases are very high and larger than 0.71. Klimenko's correlation suggests that for small values of β, the heat transfer coefficient varies with $(T_{wall} - T_{sat})^{-1/3}$ or $(T_{wall} - T_{sat})^{-1/2}$. However, for high values of β, the heat transfer coefficient is independent of wall superheat. So quantitatively, our numerical simulations have good agreement with Klimenko's correlation.

4.3. Film Boiling of Water at Near a Critical Pressure

Simulations are preformed for water at near a critical point (21.9 MPa). The properties used are given as follows: $\lambda_g = 0.538\,\text{W}/(\text{m}\cdot\text{K})$; $\lambda_l = 0.545\,\text{W}/(\text{m}\cdot\text{K})$; $\mu_g = 3.238 \times 10^{-5}\,\text{Pa}\cdot\text{s}$; $\mu_l = 4.67 \times 10^{-5}\,\text{Pa}\cdot\text{s}$; $c_{pg} = 3.52 \times 10^5\,\text{J}/(\text{kg}\cdot\text{K})$; $c_{pl} = 2.18 \times 10^5\,\text{J}/(\text{kg}\cdot\text{K})$; $\rho_g = 242.7\,\text{kg/m}^3$; and $\rho_l = 402.4\,\text{kg/m}^3$. The latent heat is $h_{lg} = 2.764 \times 10^5\,\text{J/kg}$ and the surface tension is $\sigma = 7.0 \times 10^{-5}\,\text{N/m}$. The width of the computational region is $0.5\lambda_0$ and its height is λ_0. The boundary conditions are the same as shown in Figure 4. The interface location is initialized as

$$y = \frac{\lambda_0}{128}\left(4.0 + \cos\left(\frac{2\pi x}{\lambda_0}\right)\right) \qquad (50)$$

A grid independence test was preformed by 120×240, 150×300, and 180×360 grid systems. Figure 10 depicts the interface computed as the first bubble is going
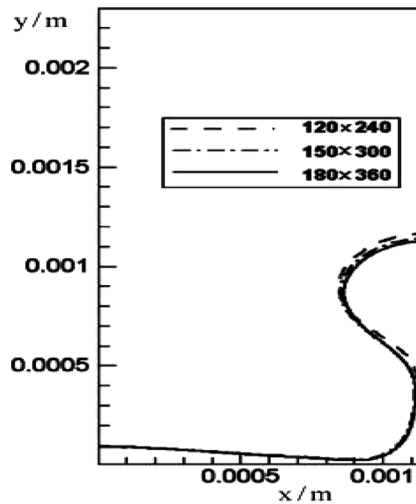

Figure 10. Bubble shape for three grid systems when the first bubble is going to leave the film.

to leave the film. According to this figure, a 180×360 grid mesh is used for later simulations. Two cases with different wall superheat are simulated.

In the first case, the temperature of the solid wall is set at $10\,\text{K}$ above the saturation temperature. The predicted periodic bubble release patterns are shown in Figure 11. With a given initial interface, a bubble is formed at the center. Then, the bubble leaves the film under the effect of buoyancy. After the detachment, the bubble still moves upwards and leaves a little vapor packet on the thin film (Figure 11*c*). The vapor packet is pulled back due to the surface tension and leads to bubble growth on the outer sides (Figure 11*f*). This cycle repeats periodically and bubble formation occurs alternatively at the center and the outer sides.

Figures 12*a* and 12*b* show the isotherms at two time instants. 1.10 s and 1.13 s. Each isotherm mainly follows the shape of the interface. Figures 12*c* and 12*d* show
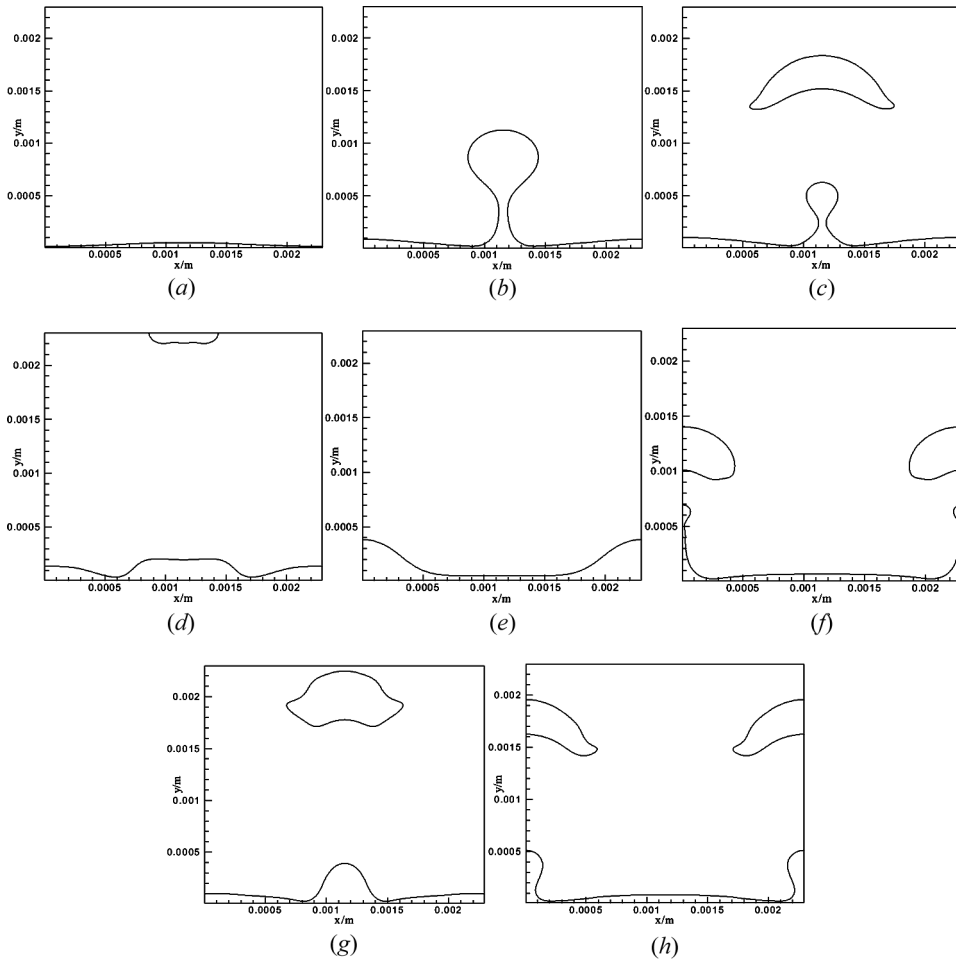
Figure 11. Bubble shapes at different instants of bubble release cycles for water with $10\,\text{K}$ superheat (*a*) t = 0.0 s; (*b*) t = 0.30 s; (*c*) t = 0.33 s; (*d*) t = 0.36 s; (*e*) t = 0.44 s; (*f*) t = 0.50 s; (*g*) t = 0.75 s; (*h*) t = 0.94 s.
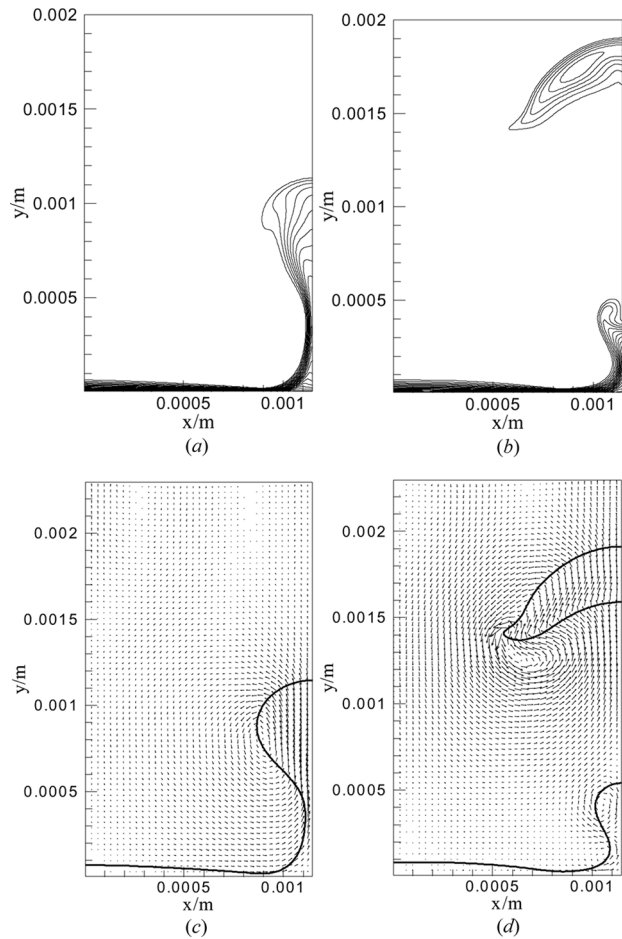
Figure 12. The isotherms (top) and velocity vectors (bottom) at two instants (*a*) t = 1.10 s; (*b*) t = 1.13 s; (*c*) t = 1.10 s; (*d*) t = 1.13 s.
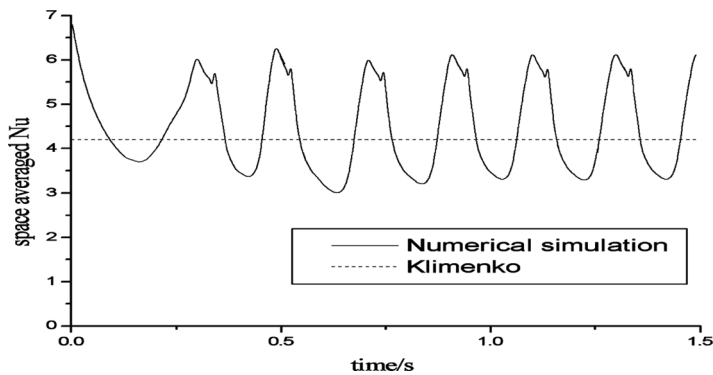

**Figure 13.** Simulation results for Nusselt number.

the velocity vectors at 1.10 s and 1.13 s, respectively. For clarity of presentation, velocity vectors are plotted every 5 grid points.

Space-averaged Nusselt numbers over time are shown in Figure 13. The computed time- and space-averaged Nusselt number is 4.67, and the Nusselt number predicted by Klimenko's correlation is 4.20. The difference is about 11.19%, and the agreement between the numerical prediction and correlation is reasonable.

The second simulation was performed with a wall superheat of 30 K. An obvious different kind of bubble behavior is found. Figure 14 describes interfaces at different time instants. For this case, tall and stable vapor columns are observed. A similar phenomenon was found in the experiments of Reimann and Grigull [29], which was presented in Dhir and Taghavi-Tafreshi [30]. The results of Reimann and Grigull [29] are copied in Figures 15a and 15b. It can be seen that the bubble is released individually and sequentially for the low heat flux situation, and columns are found for the high heat flux one. In our simulation, the heat flux is about 12 W/cm^2 for the case of 10 K superheat and 45 W/cm^2 for the case of 30 K
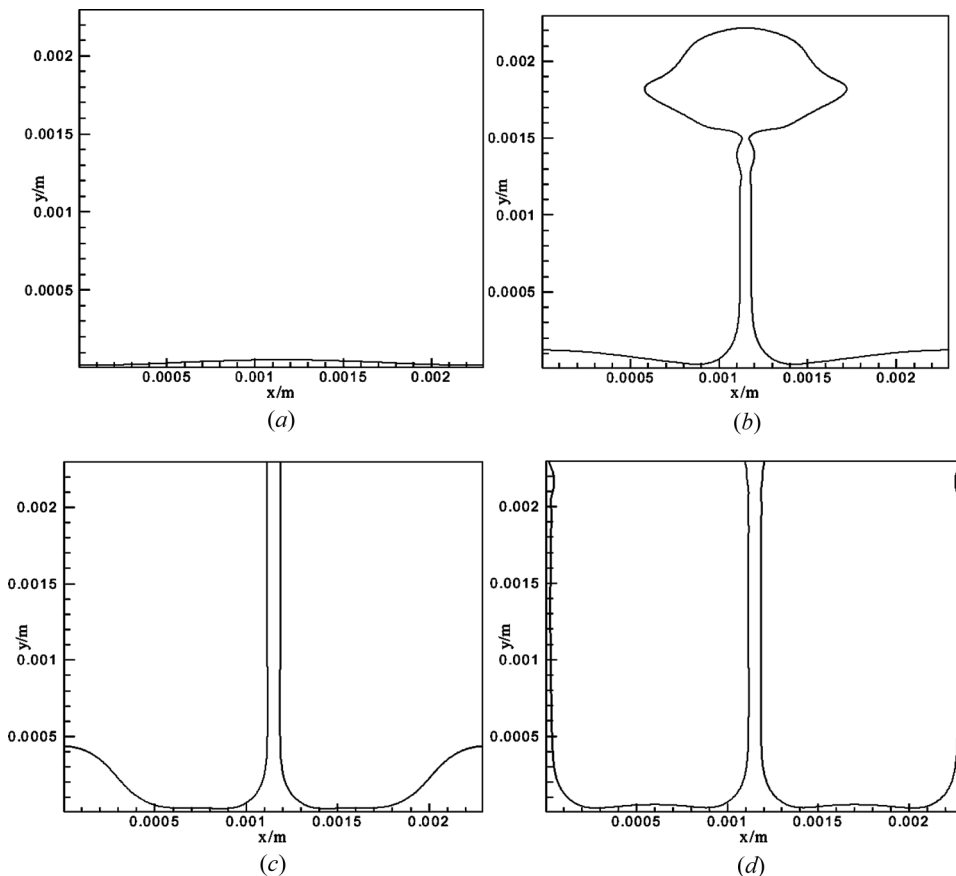
Figure 14. Bubble shapes at different instants of bubble release cycles for water with 30 K superheat (a) t = 0.0 s; (b) t = 0.27 s; (c) t = 0.40 s; (d) t = 0.54 s.

(a)   (b)
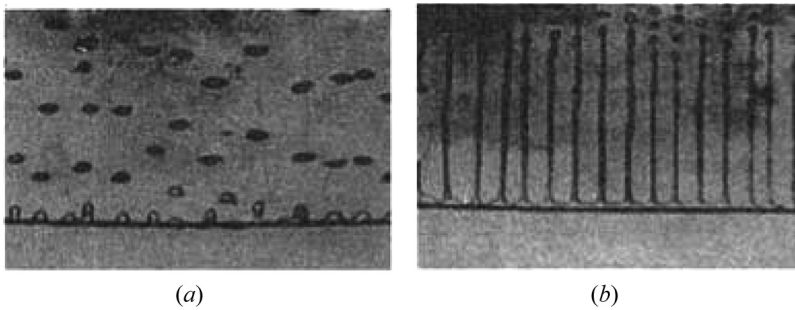
Figure 15. Experimental results of Reiman and Grigull [29]. (a) $q_w = 16.21\,\text{W}\cdot\text{cm}^{-2}$ and (b) $q_w = 27.10\,\text{W}\cdot\text{cm}^{-2}$.

superheat. Even though the predicted low and high heat fluxes are quite different from reference [29], our simulation results qualitatively agree with reference [29] very well.

5. CONCLUSIONS

In this article, the VOSET method is applied to simulate multiphase flows with phase change. This approach combines advantages of both VOF and the level set methods to capture the interface. At the interface, the velocity field is discontinuous due to phase change and the difference between the mass-weighted and volume-weighted velocities must be taken into account. Some treatment is adopted here to deal with this difference. The numerical methods and the code developed is tested by a one-dimensional Stefan problem and then applied to the simulation of two-dimensional film boiling. The predicted space-averaged Nusselt number varies with time during film boiling and its variation trend is consistent with the patterns of the bubbles' release. Simulation results of Nusselt number for all cases including water at near critical pressure are found to be in good agreement with Klimenko's correlation. In addition, the horizontal film boiling of water at near critical pressure has also been investigated with two wall superheats. Simulation results for different superheat are qualitatively agreeable with experimental observation available in the literature.

REFERENCES

1. G. Son and V. K. Dhir, Numerical Simulation of Saturated Film Boiling on a Horizontal Surface, *J. Heat Transfer*, vol. 119, pp. 525–533, 1997.
2. D. Juric and G. Tryggvason, Computations of Boiling Flows, *Int. J. Multiphase Flow*, vol. 24, pp. 387–410, 1998.
3. S. O. Unverdi, and G. Tryggvason, A Front-Tracking Method for Viscous, Incompressible, Multi-Fluid Flows, *J. Computational Physics*, vol. 100, pp. 25–37, 1992.
4. G. Son and V. Dhir, Numerical Simulation of Film Boiling Near Critical Pressures with a Level Set Method, *J. Heat Transfer*, vol. 120, pp. 183–192, 1998.
5. M. Sussman, P. Smereka, and S. Osher, A Level-Set Approach for Computing Solutions to Incompressible Two-Phase Flow, *J. Computational Physics*, vol. 114, pp. 146–159, 1994.

6. M. Sussman and E. G. Puckett, A Coupled Level Set and Volume-of-Fluid Method for Computing 3-D and Axisymmetric Incompressible Two Phase Flows, *J. Computational Physics*, vol. 162, pp. 301–337, 2000.

7. D. Enright, R. Fedkiw, J. Ferziger, and I. Mitchell, A Hybrid Particle Level Set Method for Improved Interface Capturing, *J. Computational Physics*, vol. 183, pp. 83–116, 2002.

8. M. Sussman, A Second Order Coupled Level Set and Volume-of-Fluid Method for Computing Growth and Collapse of Vapour Bubbles, *J. Computational Physics*, vol. 187, pp. 110–136, 2003.

9. C. W. Hirt and B. D. Nichols, Volume of Fluid (VOF) Method for the Dynamics of Free Boundary, *J. Computational Physics*, vol. 39, pp. 201–225, 1981.

10. S. Welch and J. Wilson, A Volume-of-Fluid Based Method for Fluid Flows with Phase Change, *J. Computational Physics*, vol. 160, pp. 662–682, 2000.

11. D. L. Youngs, Time-Dependent Multi-Material Flow with Large Fluid Distortion Numerical Method for Fluid Dynamics, in K. W. Morton and M. J. Baines (eds.), *Numer. Methods for Fluid Dynamics*, pp. 273–285, Academic, New York, 1982.

12. G. Tormar, G. Biswas, A. Sharma, and A. Agrawal, Numerical Simulation of Bubble Growth in Film Boiling using a Coupled Level-Set, and Volume-of-Fluid Method, *Physics of Fluid*, vol. 17, pp. 112103, 2005.

13. A. Bourlioux, Coupled Level-Set Volume-of-Fluid Algorithm for Tracking Material Interfaces, *Proc. of the 6th International Symposium on Computational Fluid Dynamics*, Lake Tahoe, CA, p. 15, 1995.

14. D. L. Sun and W. Q. Tao, A Coupled Volume-of-Fluid and Level Set (VOSET) Method for Computing Incompressible Two-Phase Flows, *Int. J. Heat and Mass Transfer*, vol. 53, pp. 645–655, 2010.

15. S. Osher and J. A. Sethian, Fronts Propagating with Curvature Dependent Speed: Algorithms Based on Hamilton-Jacobi Formulations, *J. Computational Physics*, vol. 79, pp. 12–49, 1988.

16. J. U. Brackbill, D. B. Kothe, and C. Zemach, A Continuum Method for Modeling Surface Tension, *J. Computational Physics*, vol. 100, pp. 335–354, 1992.

17. J. Schlottke and B. Weigand, Direct Numerical Simulation of Evaporating Droplets, *J. Computational Physics*, vol. 227, pp. 5215–5237, 2008.

18. S. V. Patankar, *Numerical Heat Transfer and Fluid Flow*, Hemisphere, Washington, D.C., 1980.

19. W. Q. Tao, *Numerical Heat Transfer*, 2nd ed., Xi'an Jiaotong University Press, Xi'an People's Republic of China, 2001.

20. L. B. Van, Towards the Ultimate Conservation Difference Scheme V, a Second-Order Sequel to Godunov's Method, *J. Computational Physics*, vol. 23, pp. 101–136, 1977.

21. D. L. Sun, Z. G. Qu, Y. L. He, and W. Q. Tao, An Efficient Segregated Algorithm for Incompressible Fluid Flow, and Heat Transfer Problems – Inner Doubly Iterative Efficient Algorithm for Linked Equations IDEAL, Part I: Mathematical Formulation and Solution Procedure, *Numer. Heat Transfer B*, vol. 53, pp. 1–17, 2008.

22. D. L. Sun, Z. G. Qu, Y. L. He, and W. Q. Tao, An Efficient Segregated Algorithm for Incompressible Fluid Flow, and Heat Transfer Problems – Inner Doubly Iterative Efficient Algorithm for Linked Equations IDEAL, Part II: Application Examples, *Numer. Heat Transfer B*, vol. 53, pp. 18–38, 2008.

23. H. A. Van Der Vorst, BI-CGSTAB: A Fast and Smoothly Converging Variant of BI-CG for the Solution of Nonsymmetric Linear Systems, *SIAM J. Sci. Stat. Comput.*, vol. 13, pp. 631–644, 1992.

24. H. A. Van Der Vorst, Efficient and Reliable Iterative Methods for Linear Systems, *J. Comput. Appl. Math.*, vol. 149, pp. 251–265, 2002.

25. V. Alexiades and A. D. Solomon, *Mathematical Modeling of Melting and Freezing Processes*, Hemisphere, Washington, D.C./New York, 1993.

26. P. J. Berenson, Film-Boiling Heat Transfer from a Horizontal Surface, *J. Heat Transfer*, vol. 83, pp. 351–358, 1961.

27. V. V. Klimenko, Film Boiling on a Horizontal Plate-New Correlation, *Inter. J. Heat and Mass Transfer*, vol. 24, pp. 69–79, 1981.

28. F. Gibou, L. Chen, D. Nguyen, and S. Banerjee, A Level Set-Based Sharp Interface Method for the Multiphase Incompressible Navier-Stokes Equations with Phase Change, *J. Computational Physics*, vol. 222, pp. 536–555, 2007.

29. M. Reimann and U. Grigull, Warmeubergang bei freier konvektion und flimsieden im kritischen gebiet von wasser und kohlendioxid, *Warmeund Stof-fubertragung*, vol. 8, pp. 229–239, 1975. (In German.)

30. V. K. Dhir, and K. Taghavi-Tafreshi, Hydrodynamic Transitions during Dripping of a Liquid from Underside of a Horizontal Tube, *ASME*, paper, 81-WA/HT-12, ASME, New York, 1981.